DEVELOPMENTAL BIOLOGY

Mechanical tension mobilizes Lgr6$^+$ epidermal stem cells to drive skin growth

Yingchao Xue[1], Chenyi Lyu[1,2], Ainsley Taylor[3], Amy Van Ee[1,2], Ashley Kiemen[4], YoungGeun Choi[2,4], Nima Khavanian[3], Dominic Henn[5], Chaewon Lee[1], Lisa Hwang[1], Eric Wier[1], Saifeng Wang[1], Sam Lee[1], Ang Li[1], Charles Kirby[1], Gaofeng Wang[1,6], Pei-Hsun Wu[4], Denis Wirtz[4], Luis A. Garza[1,7,8]*, Sashank K. Reddy[2,3,9]*

Uniquely among mammalian organs, skin is capable of marked size change in adults, yet the mechanisms underlying this notable capacity are unclear. Here, we use a system of controlled tissue expansion in mice to uncover cellular and molecular determinants of skin growth. Through machine learning–guided three-dimensional tissue reconstruction, we capture morphometric changes in growing skin. We find that most growth is driven by the proliferation of the epidermis in response to mechanical tension, with more limited changes in dermal and subdermal compartments. Epidermal growth is achieved through preferential activation and differentiation of Lgr6$^+$ stem cells of the epidermis, driven in part by the Hippo pathway. By single-cell RNA sequencing, we uncover further changes in mechanosensitive and metabolic pathways underlying growth control in the skin. These studies point to therapeutic strategies to enhance skin growth and establish a platform for understanding organ size dynamics in adult mammals.

INTRODUCTION

How metazoans establish and maintain organ size is a fundamental question in developmental biology. In mammals, organ size is largely established during development and youth with limited size change after adulthood (*1*). The skin, however, retains a remarkable capacity for growth dynamics in adult mammals. Substantial growth of skin occurs in response to increases in body mass, yet once created, new skin is not readily lost. This can be problematic as in patients with excess, overhanging skin following postbariatric weight loss (*2*, *3*). In contrast, in pregnant females, new skin created over the abdomen and chest to accommodate the demands of fetal growth and lactation largely recedes postpartum. The capacity for adult skin growth is also used therapeutically in a process known as tissue expansion. To replace skin lost to surgical resection or trauma, surgeons subcutaneously implant silicone balloons known as tissue expanders and gradually increase their size through saline injection. Similar to the induction of skin growth by an expanding fetus, the slow process of tissue expansion leads to the creation of new skin, which can be used to resurface wounds. The cellular and molecular mechanisms underpinning skin growth in these varied circumstances are of great interest (*4*–*6*), especially because skin size in homeostatic conditions is remarkably constant despite continuous turnover. Understanding these mechanisms is a prerequisite to designing therapies for conditions of excess or inadequate skin, and it may yield broader insights into size control and stimulated renewal in other adult organs.

Mammalian skin is a bilaminar structure with a multilayered epithelium overlying a dermal compartment containing fibroblasts, blood vessels, nerve endings, immune cells, and dermal appendages—hair follicles (HFs), eccrine, apocrine, and sebaceous glands. Some skin components, including epidermis and HFs, undergo homeostatic renewal throughout adult life (*7*, *8*), with distinct populations of stem cells regularly mobilized to replenish these structures. During epidermal maintenance, stem cells of the interfollicular epidermis (IFE) undergo divisions that give rise to additional stem cells and to committed keratinocyte precursors. Elegant in vivo imaging studies suggest that delamination and subsequent differentiation of basal layer precursors from the basement membrane can stimulate keratinocyte stem cell division during homeostatic renewal (*9*). A related stem cell mobilization and differentiation program underlies HF renewal in anagen, catagen, and telogen cycles (*8*). How these homeostatic processes are perturbed to create new skin in response to growth stimuli such as pregnancy or tissue expansion is unknown.

Several mechanistic questions arise. First, what morphologic changes occur in the epidermis, dermis, dermal appendages, and subdermal tissues during stimulated skin growth? Whether these subcomponents of skin grow and proliferate in concert or exhibit differential responses to growth stimuli is unknown. Second, what cells are mobilized to create new skin, and what signals drive this growth? In homeostatic conditions, skin stem cells are restricted in spatial localization and differentiation potential, yet they can exhibit lineage infidelity in circumstances such as wound healing (*10*, *11*). Defining the cells of origin for newly created skin is a critical explanatory step and will shape efforts to exploit this phenomenon therapeutically. Last, how is homeostasis restored after skin growth is complete? When growth stimuli such as tissue expansion are halted, do the pathways driving growth passively decay, or are there active brakes that retard further growth?

To investigate these broad issues, we developed a system of physiologic tissue expansion in mice that reproduces many of the features observed in human skin tissue expansion. In this system, skin growth is a local phenomenon driven by mechanical tension

[1]Department of Dermatology, Johns Hopkins University, Baltimore, MD 21231, USA. [2]Department of Biomedical Engineering, Johns Hopkins University, Baltimore, MD 21231, USA. [3]Department of Plastic and Reconstructive Surgery, Johns Hopkins University, Baltimore, MD 21231, USA. [4]Department of Chemical and Biomolecular Engineering, Johns Hopkins University, Baltimore, MD 21231, USA. [5]Department of Plastic Surgery, UT Southwestern Medical Center, Dallas, TX 75390, USA. [6]Department of Plastic and Aesthetic Surgery, Nanfang Hospital of Southern Medical University, Guangzhou 510515, Guangdong Province, China. [7]Department of Cell Biology, Johns Hopkins University, Baltimore, MD 21231, USA. [8]Department of Oncology, Johns Hopkins University, Baltimore, MD 21231, USA. [9]Institute for NanoBioTechnology, Johns Hopkins University, Baltimore, MD 21231, USA.
*Corresponding author. Email: sreddy6@jhmi.edu (S.K.R.); lag@jhmi.edu (L.A.G.)

from the expander. We find that mechanical forces drive proliferation of stem cells in the IFE, which, in turn, delaminate and differentiate to generate most of the new skin mass. Dermal and subdermal compartments demonstrate more modest proliferation in response to the same tension stimuli. Proliferation of epidermal stem cells is, in part, driven by modulation of the Hippo pathway, a major regulator of organ growth. Single-cell sequencing in the expanding epidermis identifies changes in metabolic and mechanosensitive pathways and reveals a rich target set for therapeutic manipulation. These analyses begin to define the cellular and molecular determinants of skin growth.

RESULTS

To interrogate mechanisms underlying adult skin growth, we established a system of controlled tissue expansion of back skin in mice. Small silicone tissue expanders with remote injection ports were placed in a subcutaneous, suprafascial plane in young adult mice. After 1 week of surgical recovery, saline injection into a remote port induced gradual expansion (Fig. 1, A and B). Expansion was performed over 10 days to mimic the physiologic expansion observed during normal gestation in mice, with postexpansion defined as the period after the last saline injection. To measure skin growth, we quantified the increase in surface area and weight in the skin overlying the expander. Surface area growth occurred early and rapidly during the period of serial saline injections into the expander and then slowed in the postexpansion period (Fig. 1, B and C). Weight gain in the skin overlying the expander displayed biphasic kinetics, with a gradual increase during the expansion and early postexpansion periods followed by a plateau (Fig. 1D). Given the redundancy of back skin in mice, these kinetics are consistent with a model in which the early response to expansion reflects stretching of excess skin, with subsequent tension inducing growth of newly created tissue.

We next interrogated morphologic changes in the newly created skin using our quantitative system for three-dimensional (3D) tissue reconstruction and analysis (*12*). One hundred serial 4-μm sections of hematoxylin and eosin (H&E)–stained skin samples were automatically aligned and reconstructed into 3D blocks, followed by machine learning–guided feature detection of skin subelements after algorithm training (Fig. 1, G and H; fig. S1A; and movie S1 to S4). Using this system, we found that epidermal thickness doubled in the postinjection period, with little diminution 1 month after the completion of expansion (Fig. 1I, first from the left, and fig. S1C). The dermis, by contrast, was not significantly changed in thickness during or after the expansion period compared to nonexpanded controls (Fig. 1I, second from the left, and fig. S1B). Examination of cell layers in the epidermis revealed an increase in epidermal stratification, with a two- and threefold increase of the epidermal thickness (fig. S1C) and up to eight cell layers of keratinocytes compared to two in the nonexpanded samples (fig. S1D). Keratin 10 (KRT10), which marks the differentiated/stratified epidermal cells, showed a more robust expression in expanded samples (fig. S2B). Notably, the 3D morphometrics revealed that cell density in the epidermis decreased despite the overall increase in epidermal mass, reflecting an overall increase in average cell size (Fig. 1J, left; high-magnification images were shown in fig. S1, B and D). This was particularly notable in the basal layer, consistent with individual size measurements in KRT5-positive cells (Fig. 2C). By contrast, dermal cell density increased during the expansion process, while overall dermal thickness was not significantly changed (Fig. 1, I and J; representative dermal cell density images can be found in fig. S1, B to D). Cell density in subcutaneous muscle (panniculus carnosus) was similarly unchanged after expansion, suggesting that cell growth in response to tension may be more prominent in epithelia (Fig. 1J, right, and fig. S1C).

We next examined dermal appendages, including HFs and sebaceous glands. HF numbers did not increase in response to tissue expansion (Fig. 1, E and F); hence, the existing preexpansion follicles were spaced further apart in the newly created epidermis, leading to an overall decrease in HF density (Fig. 1, F and I). The observed absence of HF neogenesis suggests that the creation of new skin in response to tissue expansion differs significantly from another well-described adult skin regeneration phenomenon—wound-induced hair neogenesis (WIHN) (*13*–*15*). Sebaceous gland volume similarly decreased during the expansion process. By contrast to the observed constancy of dermal appendages, the dermal vascular plexus grew proportionally during tissue expansion such that capillary density remained unchanged per unit of skin despite the increase in skin surface area and mass. This finding is consistent with other studies on the mechanobiology of endothelial cells during development (*16*). Together, these data suggest that various subcompartments of skin respond differentially to a common growth stimulus supplied by tension from the tissue expander.

To account for the observed increase in skin surface area and mass as well as the epidermal hyperstratification, we examined the kinetics of cell proliferation in various skin compartments. As measured by Ki67 nuclear staining, basal layer keratinocytes showed increased proliferation within 5 days after the initiation of expansion (Fig. 2A). Maximal proliferation occurred at day 14 after injection with a greater than 10-fold increase in the number of Ki67-positive cells compared to those in nonexpanded skin. This proliferation persisted following the maximum physical expansion period, with increased keratinocyte proliferation evident even 70 days following the completion of injections. The relative expression levels of epidermal stem cell markers including KRT17 and KRT5 were also increased in response to tissue expansion (Fig. 2, B and C). Fibroblast proliferation, by contrast, was not significantly elevated in expanding skin (fig. S2A). This preferential cell division of keratinocytes over fibroblasts corresponds to the thickening and hyperstratification of the epidermis without corresponding thickening of the dermis observed in our morphologic assessments (Fig. 1I and fig. S1B).

Lgr6$^+$ stem cells are major contributors to the growing epidermis

Given that most of the increased skin mass with expansion occurs in the epidermis, we wished to identify the cells of origin for this newly created tissue. Several different stem cell markers have been proposed in the epidermis, contributing to the renewal of keratinocytes, HFs, and sebaceous glands. We specifically focused on stem cells marked by Lgr5 and Lgr6 expression, which are among the most primitive stem cells characterized in epidermal development and play important roles in adult skin homeostasis (*17*–*19*). We used lineage tracing to ascertain the fate of cells marked by Lgr5 and Lgr6 during the expansion process (Fig. 3, A and B). As previously reported, Lgr5$^+$ cells [enhanced green fluorescent protein positive (EGFP$^+$)] and their descendants [tdTomato positive (tdT$^+$)] were primarily confined to the HF during homeostasis, whereas Lgr6$^+$ cells (EGFP$^+$) and their descendants (tdT$^+$) were found in both follicles and IFE (Fig. 3A and fig. S3A). We next tracked the fate and spatial distribution

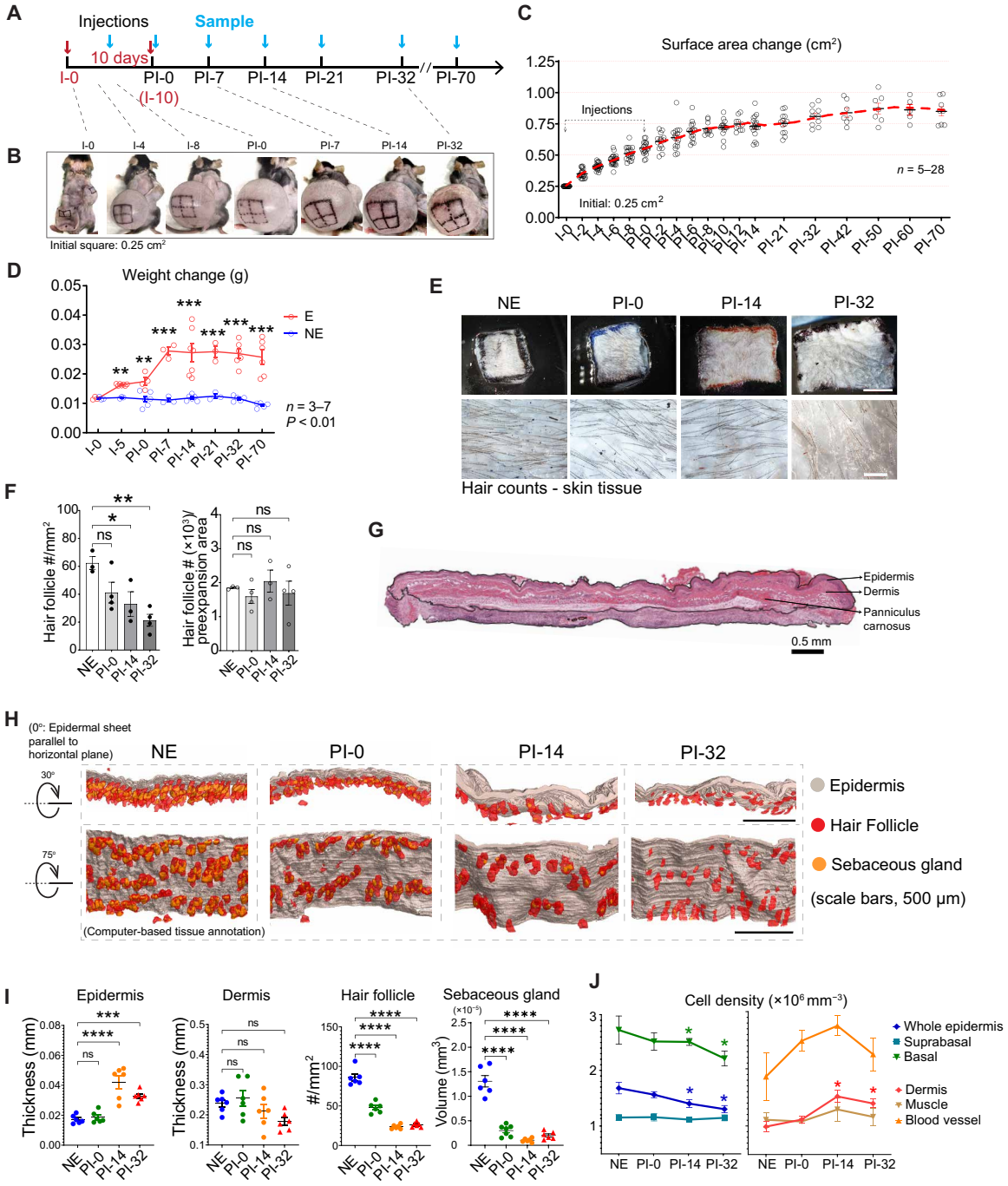

Fig. 1. Morphologic changes in skin during tension-mediated growth. (**A**) Expansion protocol. D-0, preinjection; I-#, injection day #; PI-#, post-last injection day #; E, skin overlying the inflated expander; NE, skin overlying the expander in mice where the expander was not inflated. (**B**) Gross images of mice before expansion (I-0), during expansion (I-0 to I-10), and after expansion (PI-0 to PI-32). (**C** and **D**) Skin surface area and weight changes during and after expansion. (**E**) HF identification from whole mount skin samples. Scale bars, (top row) 3 mm and (bottom row) 300 μm. (**F**) Quantification of HF density and total number in nonexpanded and expanded mice ($P < 0.01$). ns, not significant. (**G**) Assembled 3D reconstruction of 100 serial 4-μm H&E sections from expanded skin. (**H**) Automated annotation of the epidermis, HFs, and sebaceous glands in 3D skin reconstructions. (**I** and **J**) Quantification of thickness and feature density from 3D H&E skin reconstructions.

of these cells following expansion (Fig. 3C). The Lgr6-tdT cells were distributed in all layers of the epidermis (Fig. 3, C and H), including the basal, suprabasal, and cornified layers. Homeostatic skin displayed a similar distribution of these cells (Fig. 3A). Costaining of tdT with KRT5 and KRT10 showed that the Lgr6-tdT cells are located in both the basal and suprabasal/differentiated cell layers (fig. S3G). However, while Lgr5$^+$ cells and their descendants maintained their homeostatic distributions throughout the expansion period, the Lgr6$^+$ cell descendants (tdT$^+$) became widely distributed in the IFE with proportionally fewer descendants in HFs (fig. S3D).

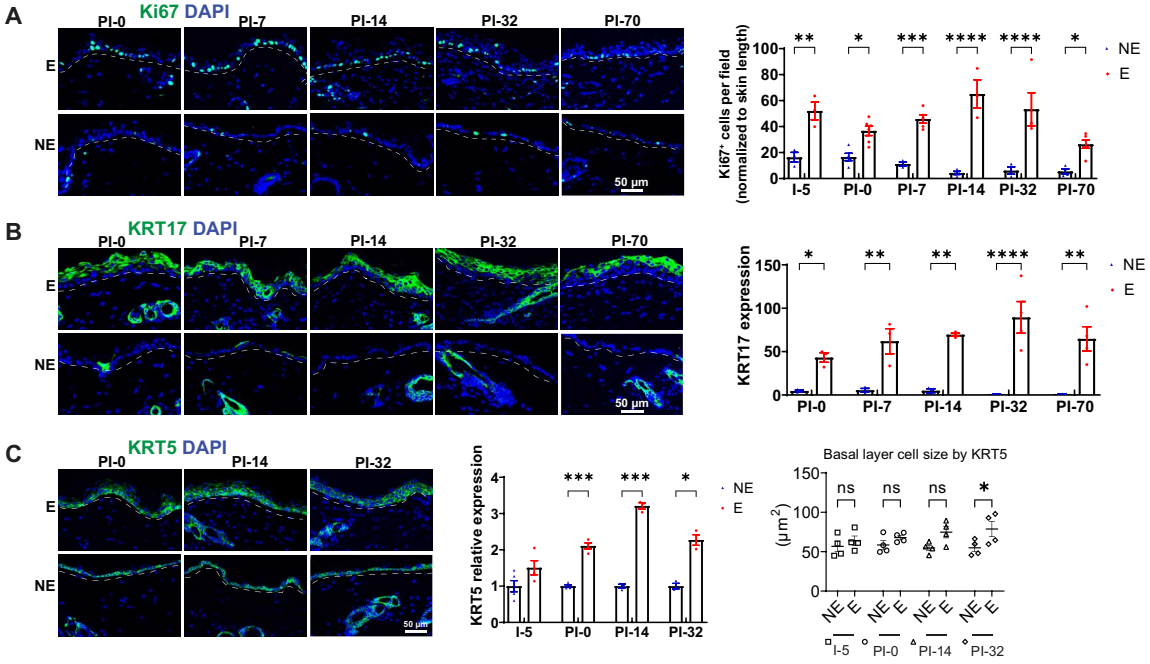

Fig. 2. Mechanical tension stimulates proliferation and stem cell activation in the epidermis. (**A**) Epidermal proliferation as measured by Ki67 immunofluorescence. (**B** and **C**) Immunofluorescence staining and quantification of epidermal stem cell markers KRT17 and KRT5 in expanded and nonexpanded skin samples. Basal layer cell sizes were quantified by using KRT5 staining to mark the cell boundary. DAPI, 4D,6-diamidino-2-phenylindole.

Costaining for Ki67 and tdT revealed that more than half of proliferating cells in the IFE were descendants of Lgr6$^+$ cells, revealing these cells as major contributors to the growing epidermis (Fig. 3, H and I, and fig. S3D). Notably, the percentage of both EGFP$^+$ Lgr5 and Lgr6 precursors declines during the expansion process, suggesting that mechanical tension biases epidermal stem cells toward differentiation rather than renewal (Fig. 3E and fig. S3, B and C). Meanwhile, the number of Lgr6-tdT descendants increased during expansion, while corresponding Lgr5-tdT cell numbers decreased (Fig. 3, D and E, and fig. S3, E and F). Pearson correlation coefficient analysis of Lgr6 EGFP$^+$ cells versus their tdT$^+$ progeny showed a negative correlation both in the entire epidermis and in the IFE specifically, further confirming that Lgr6$^+$ stem cells are biased toward differentiation during the expansion process (Fig. 3, F and G). Together, these data suggest that tension preferentially drives differentiation of Lgr6$^+$ stem cells to create new epidermis and that existing stem cell fate restrictions are respected during this process. In this way, epidermal growth during tissue expansion differs from reepithelialization during wound healing in which HF stem cells (HFSCs) migrate to the IFE and contribute to new skin (*20*, *21*).

Mechanical tension activates YAP to promote skin growth

We next considered the mechanisms by which the expansion stimulus leads to epidermal growth. We began by examining activity in the Hippo pathway, a well-known regulator of metazoan organ size that has previously been implicated in epidermal maintenance and growth (*4*, *22*, *23*). Shortly after the initiation of expansion, increased nuclear translocation of the Hippo effector YAP (yes-associated protein), but not another Hippo effector WWTR1 (TAZ), was observed in basal keratinocytes (Fig. 4A), including Lgr6$^+$ stem cells of the IFE (Fig. 4G). The proportion of nuclear YAP$^+$ cells was markedly increased in tdT$^+$ Lgr6 descendants as well (Fig. 4G). To test the functional consequence of YAP activation during tissue expansion, we generated mice expressing a Tet-inducible, constitutively active version of YAP that shows high levels of nuclear translocation—YAP^{S112A}—under the control of the basal KRT5 promoter (Fig. 4B) (*24*–*26*). As previously reported, these animals at baseline show epidermal hyperstratification upon induction of YAP^{S112A}, phenocopying the changes seen in wild-type skin upon tissue expansion (fig. S4A) (*22*). When tissue expansion was performed on induced Krt5-rtTA (reverse tetracycline-controlled transactivator);tetO (Tet operator)-YAP^{S112A} animals, skin surface area increased more rapidly and to a larger final size as compared to control animals that were expanded but not induced to express YAP^{S112A}. This increased skin growth happened shortly after induction and extended more than 1 week after expansion was completed (Fig. 4, C and D). Epidermal thickness was also increased in response to expansion in Krt5-rtTA;tetO-YAP^{S112A} transgenic animals (Fig. 4E). Consistent with these findings, we observed a higher degree of keratinocyte proliferation in the IFE in the Krt5-rtTA;tetO-YAP^{S112A} transgenic animals (Fig. 4F). To specifically interrogate the role of Hippo signaling in Lgr6$^+$ stem cells, we performed conditional deletion of *YAP* in these lineage-specific cells (Fig. 4H) and examined effects on skin growth during tissue expansion (Fig. 4I). Both surface area growth and epidermal thickness were markedly attenuated in the Lgr6^{cre};YAP^{flox} animals (Fig. 4, J to L). Moreover, the WWTR1 (WW domain containing transcription regulator 1) [TAZ (transcriptional coactivator with PDZ-binding motif)] expression level did not change in the expanded Lgr6^{cre};YAP^{flox} animals (fig. S4B), which further indicates that YAP but not WWTR1 is the essential Hippo effector during tissue expansion. Together, these data suggest that tension modulates the activity of the Hippo effector YAP to drive proliferation of keratinocyte stem cells and descendants during the creation of new skin.

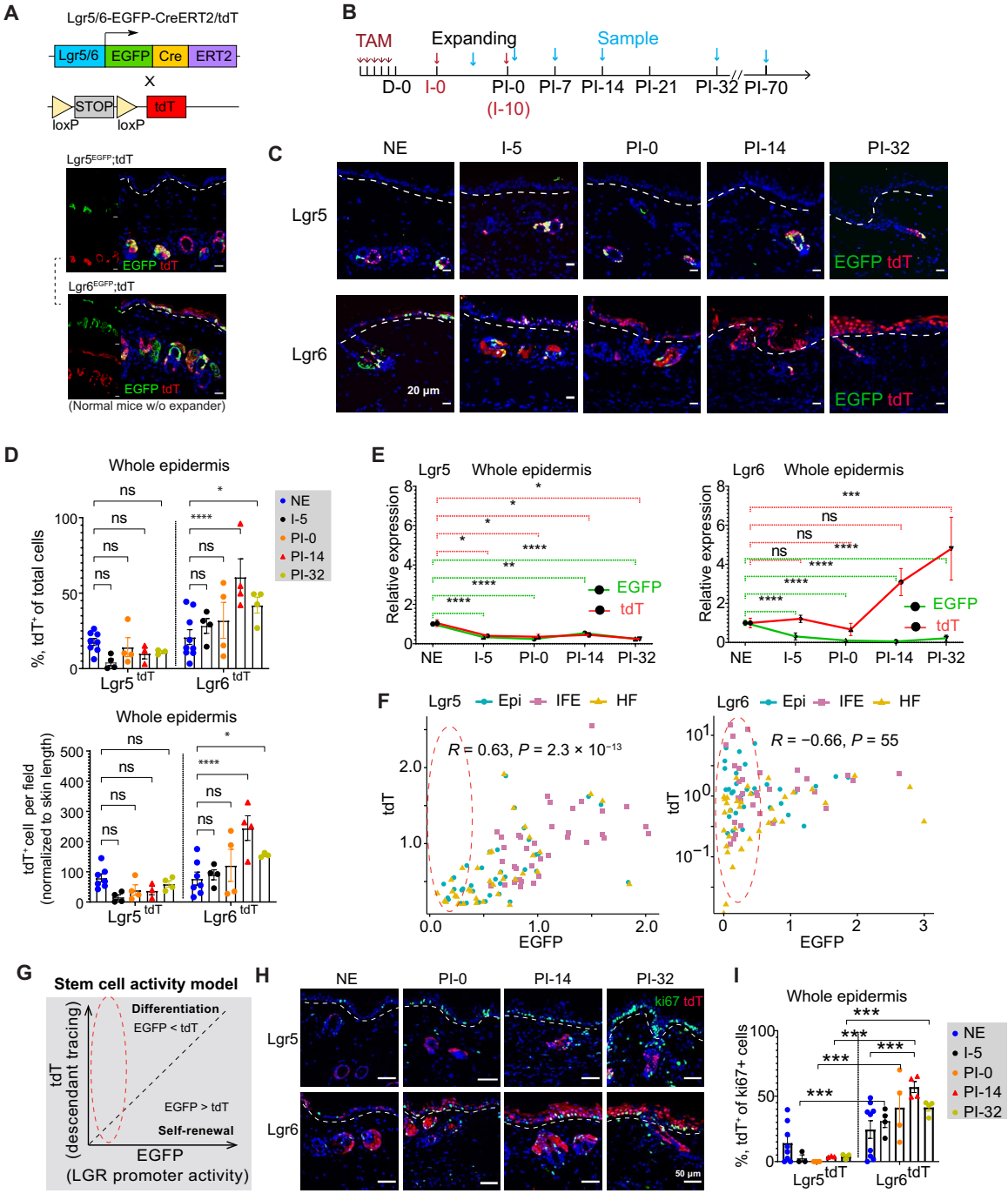

Fig. 3. Tension drives preferential differentiation of Lgr6$^+$ stem cells during skin growth. (**A**) Lineage tracing strategy for Lgr5$^+$ and Lgr6$^+$ skin stem cells and their descendants. (**B**) Expansion protocol with tamoxifen (TAM) treatment to induce tdT signal in Lgr5/6^{cre};tdT mice. (**C**) Identification of Lgr5 and Lgr6 progenitors (EGFP$^+$) and progeny (tdT$^+$) during tension-mediated skin growth. (**D**) Percentage of tdT$^+$ cells in epidermis during tissue expansion. (**E**) Relative expression of EGFP and tdT during tension-mediated skin growth. (**F**) Correlation analysis between EGFP and tdT signals in Lgr5^{cre};tdT and Lgr6^{cre};tdT mice after stretch. (**G**) Epidermal stem cell activity model based on the correlation between EGFP and tdT expression from (F). (**H**) Proliferation of Lgr5 and Lgr6 progeny as assessed by Ki67 and tdT double staining. (**I**) Percentage of proliferating cells in the entire epidermis that arise from Lgr5 or Lgr6 during expansion. tdT, tdTomato. Epi, whole epidermis. *P < 0.05.

Cellular and transcriptomic changes during skin growth

To look for additional drivers of skin growth, we collected expanded skin samples along with nonexpanded controls and performed microarray analysis on whole skin and single-cell RNA sequencing on isolated epidermal cells. Heatmap analysis of differentially expressed genes [fold change (FC) > 1.5 and FC < 0.75] in repeat samples from expanded and nonexpanded animals clustered well, suggesting the presence of a robust tension-induced skin growth transcriptome

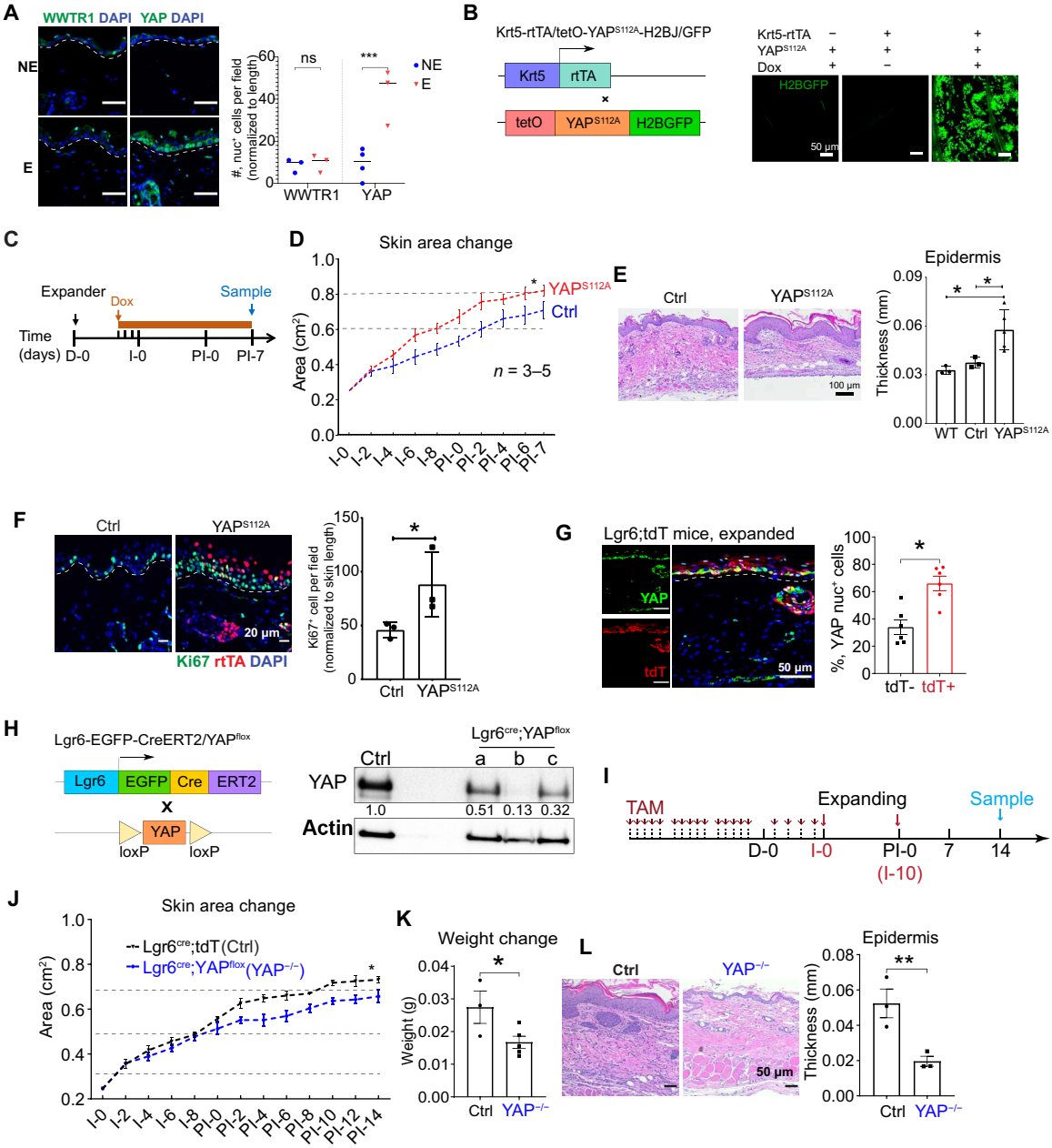

Fig. 4. YAP mediates skin growth during tissue expansion. (**A**) Immunofluorescence staining and quantification of key Hippo pathway effectors YAP and WWTR1 (TAZ) in the expanded and nonexpanded samples. Unpaired *t* test was performed. (**B**) Breeding strategy to activate YAP in Krt5^{+} skin stem cells and visualize GFP after doxycycline (Dox) feeding. Samples were obtained by ear punch. (**C**) Expansion protocol with Dox feeding to induce constitutively active YAP in Krt5^{+} keratinocyte stem cells. (**D**) Quantification of skin surface area during and after expansion in mice with and without constitutively active YAP induction. (**E**) Morphologic changes and quantification of epidermal thickness following expansion in noninduced (Ctrl) and induced (YAP^{S122A}) mice. (**F**) Quantification of proliferation in basal cells after expansion (PI-7) with and without induction of YAP^{S112A}. Ctrl: tetO-YAP^{S112A} and YAP^{S112A}: Krt5-rtTA;tetO-YAP^{S112A}. Staining: Ki67 (green) and Krt5-rtTA (red). (**G**) Lgr6 descendants (tdT^{+}) show increased nuclear YAP staining. (**H**) Breeding strategy to delete YAP in Lgr6^{+} skin stem cells by using Cre-Loxp recombination, and YAP protein level testing by Western blot after TAM treatment. (**I**) Expansion scheme in Lgr6^{cre};YAP^{flox} mice. (**J** to **L**) Decrease in skin surface area, weight, and epidermal thickness in Lgr6^{cre};YAP^{flox} mice (YAP$^{-/-}$) following tissue expansion.

program (Fig. 5A). Pathway analysis of the top 200 up-regulated genes with expansion over time revealed dynamic changes in several mechanosensitive elements, including focal adhesion and extracellular matrix (ECM) organization (Fig. 5B and table S1). Immunofluorescence imaging of the specific tension-responsive ECM proteins Integrin β1 (ITGB1) and Tenascin C (TNC) during expansion corroborated these findings from the array (Fig. 5G). Other pathways known to be activated during skin growth were also up-regulated in expanded samples, including those involved in cell migration, keratinization, calcium signaling, and tissue/skin development. Inflammatory pathways were also up-regulated in expanding skin, including cell chemotaxis, cytokine production, and tumor necrosis factor (TNF)

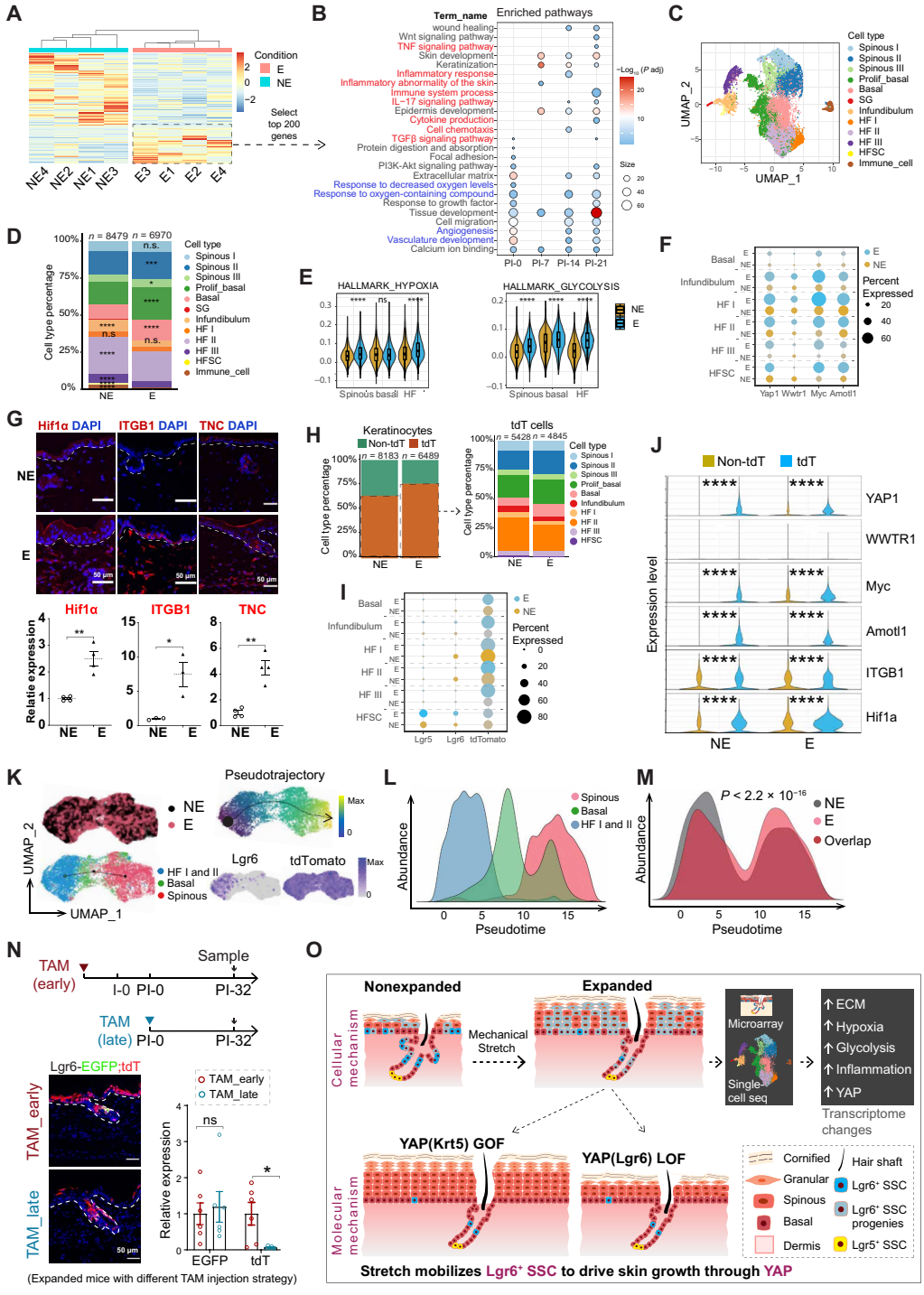

Fig. 5. Cellular and transcriptomic changes during tension-induced skin growth. (**A**) Heatmap of differentially expressed genes in expanded versus nonexpanded skin samples from the microarray. (**B**) Pathway analysis of top 200 up-regulated genes after stretch. TGFβ, transforming growth factor–β. (**C**) UMAP visualization of epidermal cells from samples isolated from the nonexpanded and expanded samples from Lgr6^{cre};tdT mice. (**D**) Representative cell components in expanded and nonexpanded samples. A chi-square test was performed (*P < 0.05, **P < 0.01, and ****P < 0.0001; n.s. > 0.05). (**E**) Gene set scoring analysis using the selected molecular signatures in the main epithelial cell types. P values are from two-sided Wilcoxon rank sum tests. **F**) Dot plot showing the expression level of YAP and its key downstream genes in each subpopulation split by sample. (**G**) Immunofluorescence staining of Hif1α, ITGB1, and TNC. Unpaired t test was performed. (**H**) Percentage of tdT$^+$ and non-tdT (tdT$^-$) cells in all keratinocytes. Bar plot showing the cell type components of tdT$^+$ cells. (**I**) Dot plot showing the expression and percentage of cells expressing Lgr5, Lgr6, and tdT in each subpopulation. (**J**) Violin plot showing the expressed level of YAP and its key downstream genes in tdT and other non-tdT cells. (**K**) Distribution of Lgr6$^+$ progenitor and Lgr6$^+$ progeny by UMAP and colored by cell type. (**L** and **M**) Cell distribution and density estimates (expanded and nonexpanded) along the inferred trajectory. (**N**) Experimental schema for early and late Lgr6 lineage cell tracing in expanded mice. Skin samples were collected on PI-32 and were immunostained with EGFP and tdT. (**O**) Graphical summary. GOF, gain of function; LOF, loss of function; SSC, skin stem cell.

and interleukin-17 (IL-17) signaling (Fig. 5B). Growth regulatory and metabolic pathways, including phosphatidylinositol 3-kinase (PI3K)–Akt signaling and response to growth factors, were similarly increased during skin growth. Consistent with these alterations in core metabolic pathways, several pathways that were known to be responsive to oxygen were altered in the arrays. We observed heightened response to decreased oxygen levels, as well as activation of pathways involved in angiogenesis and vascular development (Fig. 5B). These findings are in agreement with the increased blood vessel density observed in our 3D morphometric analysis of expanded skin (Fig. 1J). Furthermore, hypoxia-inducible factor 1α (Hif1α) protein was increased in both epidermal and dermal compartments in expanding skin (Fig. 5G and fig. S5G), raising the interesting possibility that oxygen deprivation effected by stretch may coordinate the growth of keratinocytes and the supplying vasculature (Figs. 5, B and G, and J (*27*).

Given the critical role of Lgr6$^+$ cells and their descendants in populating the newly created epidermis (Fig. 3, C and D), we performed single-cell RNA sequencing following expansion in the Lgr6^{cre};tdT mice following tdT activation (fig. S5A). After filtering out low-quality cells (fig. S5B, right), we integrated and clustered cells from all samples using Seurat (Fig. 5C). By visualizing known cell type–specific marker expression on feature plots (fig. S5C), seven major cell types emerged, including spinous cells (Krt1$^+$ and Krt10$^+$), basal cells (Krt14$^+$ and Krt5$^+$), proliferating basal cells (Mki67$^+$, Krt14$^+$, and Krt5$^+$), HF-associated cells (Krt15$^+$, Krt17$^+$, and Krt79$^+$), HFSCs (Lgr5$^+$ and Cd34$^+$), sebaceous glands (Mgst1$^+$ and Scd1$^+$), and immune cells (Cd3d$^+$ and Cd207$^+$) (Fig. 5, C and D, and fig. S5, D and E) (*28*–*30*). Cell type distribution statistics revealed that expanded samples had more cells in basal, proliferating basal, and spinous clusters (Fig. 5D), consistent with the proliferation and hyperstratification observed in expanding epidermis (Figs. 1I and 2, B and C, and fig. S1D). Moreover, we found more cells in the G_2-M cell cycle phase in the expanded samples with a corresponding decrease in quiescence scores (figs. S5B and S5, I to K).

We next compared the transcriptomic programs in expanded and nonexpanded samples. By examining the top 10 differentially expressed transcripts, we identified many inflammation-related genes, including *S100a8* and *S100a9* (*31*); the proinflammatory transcript *Stfa3* (*32*); and the keratinocyte differentiation-associated gene *Sprr2a3* (*33*). In pathway analysis, hypoxia-associated transcripts were up-regulated in expanding epidermis, consistent with the responses to decreased oxygen levels and angiogenesis seen in the microarray data (Fig. 5, E and G). Glycolytic transcripts were also up-regulated, suggesting that tissue expansion leads to alterations in metabolic pathways essential for tissue growth (Fig. 5E). Consistent with the posttranslational modulation of the Hippo pathway, we previously observed that the downstream Hippo effector *YAP1* was also up-regulated in expanding epidermis (Fig. 5F). Downstream YAP-regulated transcripts, including *Myc* and the cell migration–related gene *Amotl1*, were also elevated in expanded samples (Fig. 5F), further validating the importance of Hippo pathway signaling in skin growth. Down-regulated genes (n = 77) included those associated with cell junctions (fig. S5G), again consistent with the findings in the whole skin microarray (Fig. 5B). Wounding-related pathways scored lower in the expanded epidermis despite an elevation in wound responsive signaling in the whole skin, indicating a differential response to tension across epidermis and dermis (Fig. 5B and fig. S5H).

To examine the role of Lgr6$^+$ descendants in the expanding epidermis, we restricted the analysis to cells expressing the tdT transgene. Upon expansion, the ratio of the tdT$^+$ cells increased in the expanding skin (Fig. 5H, left), which is consistent with observations from immunostaining (Fig. 3, C to E, and fig. S3, C, E, and F). The increased number of tdT$^+$ cells was mainly located in the basal and the infundibulum groups but not the other HF groups [Fig. 5, H (right) and I]. There was a corresponding decrease in Lgr6$^+$ stem cells (EGFP$^+$) in the basal and upper HF, also consistent with previous staining (Fig. 3E). These data support a model in which tension promotes differentiation of the Lgr6$^+$ population at the expense of self-renewal during skin growth. Examination of individual genes in the Lgr6$^+$ descendants again shows that *YAP1* and its downstream effectors *Myc* and *Amotl1*, the ECM protein *ITGB1*, and the hypoxia factor *Hif1α* had higher expression levels in the Lgr6$^+$ descendants (tdT) as compared to nondescendants (non-tdT). Furthermore, the expression of these transcripts was higher in expanded samples compared to nonexpanded controls (Fig. 5J). Together, these results confirm the importance of Lgr6$^+$ cell differentiation in growing skin (Fig. 3 and fig. S3).

Pseudotime analysis reveals that Lgr6$^+$ stem cells adapt early to mechanical tension

To assess the lineage trajectory of Lgr6 cells (EGFP$^+$ and/or tdT$^+$) during tension-mediated growth, we next modeled their gene expression dynamics by ordering them on a pseudotemporal axis (Fig. 5K). We first identified cell populations that had the highest levels of Lgr6$^+$ (EGFP$^+$) cells and their descendants (tdT$^+$). We found that Lgr6$^+$ cells were mainly located in the basal, HF I, and HF II populations, while tdT$^+$ cells were distributed in all cell types as displayed on the principal components analysis plot (Fig. 5K). The integrated uniform manifold approximation and projection (UMAP) showed a similar distribution of cells in the expanded and nonexpanded samples, with the cells showing robust tdT expression and the Lgr6$^+$ skin stem cells (EGFP$^+$) accumulating at the pseudotime trajectory starting point (Fig. 5K, left). The global path along the development axis was well balanced (Fig. 5K, top left), enabling us to fit a global trajectory to the full dataset before downstream analysis (*34*). We next examined cell distribution along the pseudotime trajectory (Fig. 5L). Cell density estimation distribution for the two samples showed a bimodal distribution for both expanded and nonexpanded samples (Fig. 5M). Pseudotime values with cell distribution showed a significant difference between the two conditions (Fig. 5M), with a greater abundance of expanded cells supporting their roles as key contributors to tension-dependent growth.

We next examined the expression changes of genes known to be involved in epidermal development (*35*) along the pseudotime axis. The expanded group showed greater expression changes of basal cell and bulge marker genes early in pseudotime. For example, IFE basal cell signature genes like *Ifitm3* (P = 0) reached their peak expression at an earlier time and then decreased along the pseudotime axis as did other basal cell genes like *Krt14* (P = 0) (fig. S5K). Bulge genes *Sparc* (P = 0) and *Postn* (P = 0) also rise early along the pseudotime trajectory (fig. S5K). These pseudotime results suggest that tissue expansion activates markers of epidermal stem cells early, with subsequent rapid loss of these markers as these cells differentiate—consistent with our findings of increased differentiation/stratification and a thicker epidermis at later time points after expansion. To experimentally test the hypothesis that expansion preferentially mobilizes stem cells early during skin growth, we traced the fate of Lgr6-EGFP cells before expansion [injection day 0 (I-0)]

and after expansion (PI-0) (Fig. 5N). As expected, we found that the final distribution of Lgr6-EGFP stem cells was not affected by the tracing strategy. By contrast, when their descendants were examined, tdT^+ cells in newly grown epidermis were almost exclusively derived from Lgr6 stem cells present before the application of mechanical tension (Fig. 5N). Collectively, these data suggest that during expansion, $Lgr6^+$ cells in the epidermis rapidly expand, activate, and differentiate to drive skin growth (Fig. 5O).

DISCUSSION

While mechanisms underlying homeostatic renewal of mammalian skin have been intensely investigated, comparatively little attention has been paid to principles governing skin growth (*9*, *36*, *37*). The remarkable capacity of adult skin to grow in physiologic, pathophysiologic, and therapeutic contexts makes it an ideal organ for studying size control mechanisms. Here, we used a miniature tissue expansion system to effect localized growth in murine skin. This system allows us to uncover morphologic and molecular changes governing size dynamics in the skin.

Growth stimuli are interpreted differently by heterogeneous skin compartments

Skin-resident stem cells are tightly regulated during homeostatic renewal and in response to damage, ensuring that the complex architecture of the skin is preserved (*8*, *38*). How these cells respond to tension-mediated growth perturbations is unclear. Using quantitative 3D tissue reconstructions, we find that epidermal mass increases significantly in response to tissue expansion, with marked keratinocyte proliferation during and after maximal skin stretch. While both IFE and HFs are capable of homeostatic renewal, only the IFE exhibits significant tension-mediated growth. The absence of HF neogenesis in this system is likely a consequence of the more limited tissue damage induced by the expander as compared to the full thickness wounds necessary to incite WIHN and is reflected in the partial overlap of pathways important for WIHN and expander-driven growth Fig. 5B (*13*–*15*). In the dermis, fibroblast proliferation is only mildly elevated during expansion, while subdermal capillary growth is more marked. These findings suggest that varied precursor/stem cells throughout skin compartments interpret growth stimuli differently, yet some level of coordination must be preserved to ensure functional organ growth. At the extreme, growth in the epidermis without corresponding growth in the dermis and vasculature would result in dysfunctional or nonviable tissue architecture. How coordination between disparate stem cells is established during skin growth is an important area for future investigation. Furthermore, strategies to tune the growth of individual cell types may improve clinical tissue expansion. For example, skin breakdown and exposure of expanders—a major problem plaguing stimulated skin growth in therapeutic contexts—may be ameliorated if fibroblast proliferation and dermal thickness matched growth in the overlying epidermis.

Tension promotes activation of $Lgr6^+$ stem cells

Several tissue-resident stem cells have been identified in the epidermis, with those marked by Lgr5 and Lgr6 expression being among the earliest to arise during development. In adult skin, while $Lgr5^+$ cells are primarily confined to the HF bulge and participate in HF renewal, $Lgr6^+$ cells are present in both IFE of dorsal and volar skin and in HFs (*17*, *39*). Despite their close developmental overlap, these cells show a marked difference in response to tension with Lgr6 descendants proliferating throughout the IFE and constituting a significant portion of new skin mass. By contrast, Lgr5 descendants are confined to HFs, which themselves do not increase in number in this system. Furthermore, both stem cell types respect their predestined lineage commitments, with almost no Lgr5 descendants contributing to the expanding IFE. Activation of these stem cells in response to tension thus differs from mobilization following wounding where lineage infidelity is observed (*10*, *11*). While descendants of Lgr6 cells are found throughout the IFE, the number of $Lgr6^+$ stem cells themselves declines during tissue expansion (Figs. 3, C and E, and 5O). Tension, therefore, seems to promote differentiation of $Lgr6^+$ epidermal stem cells at the expense of self-renewal, as has been observed in other skin growth contexts (*4*). How the critical $Lgr6^+$ stem cell population recovers during restoration of skin homeostasis is a key question for future exploration. $Lgr6^+$ stem cells are critical precursors for rare regenerative events in mammals including WIHN and digit tip regeneration (*17*, *40*, *41*). Together with the findings here, these observations identify $Lgr6^+$ cells as key determinants of growth and regeneration in mammals.

Signals driving skin growth

Using both candidate and discovery approaches, we uncovered a number of pathways that mediate skin growth. First, we identified the Hippo pathway, a major regulator of cell and organ size, as a driver of skin growth. As previously seen in epidermal homeostasis and response to tension (*4*, *42*), nuclear translocation of the Hippo effector YAP drives keratinocyte proliferation in response to tissue expansion (Fig. 4). YAP nuclear translocation is tension responsive in several systems (*43*, *44*). Given that Lgr6 cells populate the IFE and the HFs (*40*), whereas Lgr5 cells are localized the follicle bulge alone, these data raise the intriguing possibility that local differences in tension within distinct epidermal compartments underlie differential growth responses (Fig. 5O). YAP nuclear translocation has also been shown to promote proliferation of fibroblasts and endothelial cells (*45*). Differential sensitivity to Hippo pathway activation in various skin cell types may underlie the differential tension-responsive growth observed in our morphometric studies (Fig. 1). More broadly, different intrinsic set points of a common pathway may afford one way to coordinate precursor cell activity during organ growth.

In addition to classical tension-responsive elements such as the Hippo pathway and ECM-receptor interactions, additional growth regulators emerged from the arrays. Inflammatory signaling has been shown to contribute to regeneration in several systems (*46*). In our analysis, several inflammatory pathways—including IL-17, TNF, transforming growth factor–β, and chemokine and cytokine signaling—were up-regulated during skin growth (Fig. 5B). In a related system for murine skin stretching, macrophage polarization was found to be a critical driver of HF renewal (*47*). Inflammatory signatures were also increased in a system of hydrogel-mediated skin expansion, although treatment with topical corticosteroids did not preclude epidermal proliferation (*4*). In earlier work from our laboratory, Toll-like receptor 3 and IL-6 signaling were markedly proregenerative in murine skin (*13*). The roles of specific inflammatory cells and signaling pathways in promoting skin growth are an important area for future investigation. Perturbation of these pathways with approved immunomodulatory agents may afford additional pathways for

enhancing skin growth. Last, we find several alterations in energy sensing and metabolic components, including PI3K-Akt, Hif1α, and glycolysis (Fig. 5E and fig. S5G). Signaling through the PI3K-Akt axis has been shown to regulate cell growth in several systems (*48*–*50*). Akt signaling can also directly up-regulate Hif1a (*51*, *52*). As Hif1α is also known to promote glycolytic metabolism (*53*), the coordinated up-regulation of these pathways suggests a common metabolic program activated during tension-responsive growth. Oxygen deprivation (Fig. 5B) by the expander may also act as an independent signal promoting proliferation of skin cells in addition to direct mechanotransduction. Hence, this metabolic program affords another set of targets by which to enhance skin growth.

Therapeutic implications

Conditions of excess or inadequate skin abound in clinical medicine, from postbariatric weight loss to burns to chronic wounds associated with diabetes, venous stasis, and frailty. While tissue expansion is a powerful tool to create new skin, its use has been limited by a poor understanding of the cellular and molecular underpinnings of skin growth. By defining the differential responses of skin elements to tension-dependent growth, we begin to identify targets to improve skin generation. Specifically, methods to promote fibroblast proliferation to keep pace with epidermal growth may lead to more effective expansion. Increasing the number of $Lgr6^+$ stem cells may also lead to more robust growth in the epidermis as it could offset the depletion of these cells seen during expansion, which is feasible by autologous cell therapy (*54*–*56*). An exciting possibility is that direct activation of tension-responsive elements such as YAP may enhance skin growth with tissue expanders or obviate the need for expanders altogether. A number of small-molecule modulators of the Hippo pathway have been described and can be tested during stimulated skin growth (*57*, *58*). Furthermore, we find several up-regulated pathways in inflammatory signaling, oxygen sensing, and metabolism that afford additional molecular targets for enhancing skin growth. Last, given the role of Lgr-marked cells in other hierarchically organized tissues, our data raise the intriguing possibility that mechanical signals may drive growth in other organs such as the gut and lung (*59*, *60*).

MATERIALS AND METHODS

Mice

All mouse experiments were approved by the Johns Hopkins University Animal Care and Use Committee (IACUC) and abided by the IACUC protocols, and animals were maintained in the Johns Hopkins School of Medicine animal facilities. All mouse backgrounds are based on C57BL/6. DNA was extracted from the digit tips from young pups or the tail tip in adult mice followed by polymerase chain reaction for genotyping.

Lineage tracing mouse model

To allow for lineage tracing of $Lgr5/6^+$ SCC progeny, the tissue expansion model was applied on Lgr5/6-EGFP-CreERT2;tdT mice. Before the subcutaneous insertion of the expander [(D-0)], five tamoxifen (TAM) injections (100 mg/kg per day) were given daily intraperitoneally (Lgr5-cre mouse line: JAX, no. 008875; Lgr6-cre mouse line: the Jackson Laboratory, no. 16934; and tdT reporter line: the Jackson Laboratory, no. 007909).

YAP gain- and loss-of-function mice model

To activate YAP in $Krt5^+$ skin stem cells, we fed the Krt5-rtTA; tetO-YAP^{S112A} mice and control mice with a doxycycline diet (200 mg/kg; Bio-Serv) starting from 3 days before I-0. The Krt5-rtTA mouse strain is a gift from S. Millarin of the Icahn School of Medicine at Mount Sinai (tetO-YAP^{S112A} mouse line: JAX, no. 031279).

YAP loss-of-function model

To delete YAP protein specifically in $Lgr6^+$ skin stem cells, the $Lgr6^{Cre}$;YAP^{flox} mice were treated with TAM intraperitoneally (100 mg/kg per day) five times a week, for a total of 4 weeks ($YAP^{fl/fl}$ mouse line: JAX, no. 027929).

Tissue expansion model protocol

Mice were anesthetized with volatile anesthesia (Baxter, Isoflurane). Using surgical scissors, a transverse cut was made into the dorsal skin below the neck of adult mice (8 to 9 weeks, around 24 g), allowing for the insertion of a silicon expander (PMT Corporation, catalog no. 3611-376) subcutaneously on D-0. This incision was then sutured, and after allowing for 7 days of recovery, 4 ml of phosphate-buffered saline (PBS) was injected every 2 days for 10 days to achieve a total volume of 24 ml (I-0 to I-10). For the control mice, expanders were implanted, but no PBS injections were administered, and, subsequently, there was no applied mechanical stimulation. A 0.25 cm^2 square was marked on I-0 on the skin above the expander. The dimensions and mass of this square of tissue were measured throughout the expansion protocol. All procedures were performed under the biological safety cabinet of Johns Hopkins School of Medicine.

Sample collection

For histology, skin samples were fixed in 4% paraformaldehyde overnight and then transferred to PBS. These biopsies were then sent to the Johns Hopkins Oncology Tissue Services Core facility to be embedded in paraffin, sectioned into 4-μm-thick segments, mounted onto glass slides, and stained with H&E.

3D skin reconstruction

3D reconstruction method for serial tissue sections

Four conditions (control, day 0, day 14, and day 32 after injection) were selected for 3D reconstruction and analysis. For each condition, three biological repeats and two technical repeats were performed for a total of 24 tissue samples. Each sample was serially sectioned into 100 4-μm-thick sections, stained with H&E, and scanned at 20× resolution. Using CODA, a method for 3D reconstruction and multilabeling of serial tissue sections further described in (*61*), the samples were visualized and analyzed.

Briefly, 3D reconstruction using CODA is accomplished as follows. The components of the 3D reconstruction are as follows. (i) Image registration: Serial images were aligned to a common coordinate system using nonlinear image registration. The registration approach relies on maximizing the cross-correlation of smoothed, down-sampled images and their radon transforms. (ii) Cell detection: Following registration, cell coordinates were determined through color deconvolution and a 2D pixel intensity maximum localization algorithm. Unsupervised *k*-means clustering is used to deconvolute the two stains in H&E images. (iii) Tissue multilabeling: Next, the H&E images were multilabeled for the epidermis, basal layer, stratum corneum, HFs, sebaceous glands, collagen, panniculus carnosus, and blood vessels using a deep learning semantic segmentation algorithm relying on convolutional neural networks. (iv) Visualization and quantification: The deep learning model is based on manual annotations of tissue components recognizable by pathologists in H&E images. Models were trained and

validated on manual annotations until a class precision and recall of 85% were obtained.

Quantification of serial tissue section samples

Labeled, registered digital tissue volumes were used to visualize and quantify changes to mouse skin following expansion. Epidermal thickness was quantified by calculating the minimum distance between regions classified as collagen/basement membrane and areas classified as the outer edge of the epidermis for each image. Dermis thickness was quantified by calculating the minimum distance between the panniculus carnosus and the inner edge of the epidermis for each image. HF density was determined by calculating the distinct volumes classified as HFs by the deep learning algorithm. Where HFs were very densely packed, they were manually counted to ensure accuracy. We used the ruler function in Aperio ImageScope to quantify cell nucleus size. Cell density variation across conditions was measured by assessing the number of cells and overall tissue volume of the epidermis. The mean and SE of the epidermis thickness, dermis thickness, HF density, and sebaceous gland density were determined and plotted for each case. All 3D reconstruction methodology, visualization, and quantification were done using MATLAB 2020A.

HF density quantification by whole skin tissue

To quantify the density of HFs, we obtained images of the skin tissue using a dissecting microscope (Olympus). The tissue area was first measured using ImageJ, after which the number of HFs found in the sample was quantified by counting the number of hair shafts. This frequency was then divided by the area to find the density.

Immunofluorescence staining

Frozen skin tissue sections were first deparaffinized, after which heat-induced antigen retrieval was performed. After permeabilization in 0.2% Triton X-100 in tris-buffered saline (TBS) and washing in TBS, a blocking buffer (5% goat serum and 1% bovine serum albumin) was applied. For mouse-on-mouse staining, unconjugated affinity-purified Fab fragment anti-mouse immunoglobulin G (IgG) (H+L) was applied and incubated for 1 hour at room temperature to block endogenous IgG. Otherwise, the sections were then incubated with primary antibodies at 4°C overnight. After additional washing, the samples were then incubated with secondary antibodies conjugated with fluorescent dye for 2 hours at room temperature in the dark. After a final round of washing, we mounted the tissue sections with ProLong Gold Antifade Mountant with 4w,6-diamidino-2-phenylindole (Thermo Fisher Scientific, P36931). Primary antibodies used were as follows: anti-Ki67 (1:500; Abcam, ab15580; rabbit), anti-KRT17 (1:1000; Abcam, ab53707; rabbit), anti-KRT5 (1:300; Abcam, ab52635; rabbit), anti-YAP [rabbit; 1:100 for IF (immunofluorescence) and 1:1000 for Western blot; Cell Signaling Technology (CST), 14074T], anti-TAZ (transcriptional coactivator with PDZ-binding motif) (rabbit; 1:100; CST, V386), anti-tdT (rabbit; 1:400; Rockland Immunochemicals, 600-401-379), anti-GFP (chicken; 1:500; Aves, GFP-1020), anti-Hif1a (mouse; 1:200; Abcam, ab1), anti-goat anti-mouse Fab (goat; 1:100; Abcam, ab6668), anti-tdT (goat; 1:400; dsRED; Mybioscience.com, MBS448092), anti-Integrin β1 (ITGB1), (goat; 10 μg/ml; R&D Systems, AF2405), anti-Tenascin C (TNC) (rat; 10 μg/ml; R&D Systems, MAB2138-SP), and anti-vimentin (mouse; 1:50; Santa Cruz Biotechnology, sc-6260). All tissue slides were imaged using fluorescence microscopy (Leica microsystems, Zeiss LSM 800 GaAsP). Quantification was performed with ImageJ.

Western blot

Skin samples were treated with 0.4% dispase II solution at 4°C overnight. The epidermal sheets were separated from the dermis manually and treated with 0.25% trypsin/EDTA at 37°C for 5 min. Cell suspensions were filtered through a 70-μm filter, and cell pellets were collected for protein analysis. Twenty micrograms of protein was loaded for electrophoresis and transferred onto the polyvinylidene difluoride membrane. After blocking with 5% dry milk for 1 hour at room temperature, the membrane was incubated with primary antibody YAP in 4°C overnight and then incubated with secondary antibody for 1 hour at room temperature. For β-actin, the horseradish peroxidase (HRP)–conjugated antibody was incubated at room temperature for 1 hour. Last, proteins were visualized using a SuperSignal West Pico PLUS chemiluminescent substrate kit (Thermo Fisher Scientific, no. 34577) and saved as image files using ChemiDoc XRS+ (Bio-Rad). Protein levels were normalized to β-actin (mouse; 1:10,000; Thermo Fisher Scientific, MA5-15739-HRP) for quantification. The signal intensity of protein was quantified using ImageJ software (https://imagej.nih.gov/ij/download.html).

Microarray

According to the manufacturer's protocols, RNA isolated from mouse skin samples were submitted to the Johns Hopkins Medical Institution (JHMI) Deep Sequencing and Microarray core for Affymetrix Human Exon 1.0ST and mouse microarray chip. Raw gene expression signals in Affymetrix CEL files were extracted and normalized with Partek Genomics Suite software using the robust multichip analysis algorithm. Genes were ranked according to fold change of the intervention and referred to as top or bottom induced if they are at the highest fold change (top) or lowest fold change (bottom).

Single-cell RNA sequencing

Cell isolation and live cell selection

Skin samples were incubated in 0.4% dispase II solution at 4°C overnight. Epidermal sheets were separated from the dermis manually on the next day and digested in 0.25% trypsin/EDTA to obtain single cells (*62*). Isolated cells were then stained with propidium iodide (PI)/dye cycle violet (DCV) for flow cytometry sorting for single live cells in the flow cytometry core at the Johns Hopkins School of Public Health. PI^-/DCV^+ single live cells were selected and submitted to JHMI Deep Sequencing and Microarray Core for single-cell sequencing.

Data preprocessing and quality control

We have two batches of data for a total of four samples, with each sample consisting of three biological replicates. After the initial cell ranger metric assessment, data were preprocessed with the Seurat package (*63*). We kept cells with more than 500 unique molecular identifiers (UMIs), 200 genes, 0.7 cell complexity ($\log_{10}$ gene per UMI), and less than 0.1 mitochondria gene ratio and filtered out genes that were expressed in fewer than 10 cells.

After quality control, 15,802 cells with 17,022 genes remained and were used for clustering. Briefly, single-cell data matrices were first normalized and log-transformed. Cell cycle phases were calculated and assigned using the software's CellCycleScoring function for each sample. To remove unwanted sources of variability caused by differences in cycling stages and mitochondrial ratio, we set the variable.features.n to be 3000 and included mitoRatio, S.scores, and G_2-M.score in vars.to.regress. Next, to ensure that similar cells across the conditions were clustered, we used the top 3000 highly variable

genes for canonical correlation analysis implemented in Seurat to align and integrate the entire dataset. Principal components analysis was performed first, and the top 20 of 40 principal components with resolution 0.45 were selected to obtain 16 clusters. By visualizing the established epithelial cell markers from the literature on the feature plot, we identified 13 clusters for downstream analysis. All details of the Seurat analyses performed in this work can be found in the website tutorial (https://satijalab.org/seurat/v3.0/pbmc3k_tutorial.html, https://github.com/hbctraining/scRNA-seq_online/tree/master/lessons).

Gene set enrichment analysis and gene ontology analysis

Gene ontology analysis of differentially expressed genes was performed by gprofiler2 (https://biit.cs.ut.ee/gprofiler/page/r) (*64*). Representative terms were selected from top-ranked gene sets/pathways. All differentially expressed genes were first evaluated by the Wilcoxon rank sum test (by wilcoxauc function in presto). The queried databases included Molecular Signatures Database (MSigDB): canonical pathway (CP) KEGG, CP REACTOME, and Hallmark.

Gene scoring analysis

We acquired gene sets from the MSigDB and published literature to calculate gene scores for selected molecular signatures. The AddModuleScore function in the Seurat R package was then used to calculate the average expression level of each gene set for each cluster on a single-cell level. The two-sided Wilcoxon rank sum test was adapted to determine whether there was a significant difference between the evaluated signature scores of the two groups.

Pseudotime and trajectory inference

We adopted the analysis procedure from an online resource (https://kstreet13.github.io/bioc2020trajectories/articles/workshopTrajectories.html). We performed pseudotemporal ordering of $Lgr6^+$ (progenitor) and tdT^+ (Lgr6 progeny) cells, including spinous cells, nonproliferating basal cells, infundibulum, and HF I and HF II cells (the HF subtypes enriched for $Lgr6^+$ stem cells). Briefly, we assessed the imbalanced score, which helps determine whether local cell distribution is balanced compared to global cell distribution. We applied the Kolmogorov-Smirnov test on the derived pseudotime values with cell distribution ($P < 2.2 \times 10^{-16}$) to compare the differences between the two conditions. Next, we performed trajectory inference using cells from both conditions in Slingshot. We looked for genes that (i) change in gene expression along the pseudotime trajectory and (ii) are differentially expressed between the two conditions along the trajectory. The differential expression (DE) analysis used the Bioconductor package tradeSeq. We use (i) associationTest function to test the gene expression changes along the pseudotime and found that 1314 genes for nonexpanded sample and 991 genes for expanded sample (836 genes are overlapped) showed significance in this test and (ii) use conditionTest function in tradeSeq to test DE between conditions. The criteria of significant DE genes are with adjusted $P < 0.05$ and with a fold change higher than 2 or lower than 0.5. We discovered 441 DE genes. The null hypothesis was used to test whether the gene expression change with the pseudotime was significant.

Statistics

All in vivo and in vitro experiments were performed in at least three individual instances. The Student's *t* test or one-way analysis of variance (ANOVA) was used to perform univariate statistical analysis. For multivariate analyses, the one-way ANOVA test was used. Statistical significance was defined on the basis of $^*P < 0.05$, $^{**}P < 0.01$, $^{***}P < 0.001$, or $^{****}P < 0.0001$, as indicated in the figures. These tests were performed using GraphPad Prism Software (GraphPad Software). Data are represented as means ± SEM.

SUPPLEMENTARY MATERIALS

Supplementary material for this article is available at https://science.org/doi/10.1126/sciadv.abl8698

View/request a protocol for this paper from *Bio-protocol*.

REFERENCES AND NOTES

1. J. Parker, G. Struhl, Control of *Drosophila* wing size by morphogen range and hormonal gating. *Proc. Natl. Acad. Sci. U.S.A.* **117**, 31935–31944 (2020).
2. J. Wilding, Weight loss is the major player in bariatric surgery benefits. *Nat. Med.* **26**, 1678–1679 (2020).
3. G. Fruhbeck, Bariatric and metabolic surgery: A shift in eligibility and success criteria. *Nat. Rev. Endocrinol.* **11**, 465–477 (2015).
4. M. Aragona, A. Sifrim, M. Malfait, Y. Song, J. van Herck, S. Dekoninck, S. Gargouri, G. Lapouge, B. Swedlund, C. Dubois, P. Baatsen, K. Vints, S. Han, F. Tissir, T. Voet, B. D. Simons, C. Blanpain, Mechanisms of stretch-mediated skin expansion at single-cell resolution. *Nature* **584**, 268–273 (2020).
5. X. Liang, X. Huang, Y. Zhou, R. Jin, Q. Li, Mechanical stretching promotes skin tissue regeneration via enhancing mesenchymal stem cell homing and transdifferentiation. *Stem Cells Transl. Med.* **5**, 960–969 (2016).
6. J. Ding, L. Lei, S. Liu, Y. Zhang, Z. Yu, Y. Su, X. Ma, Macrophages are necessary for skin regeneration during tissue expansion. *J. Transl. Med.* **17**, 36 (2019).
7. E. Fuchs, H. M. Blau, Tissue stem cells: Architects of their niches. *Cell Stem Cell* **27**, 532–556 (2020).
8. S. Dekoninck, C. Blanpain, Stem cell dynamics, migration and plasticity during wound healing. *Nat. Cell Biol.* **21**, 18–24 (2019).
9. K. R. Mesa, K. Kawaguchi, K. Cockburn, D. Gonzalez, J. Boucher, T. Xin, A. M. Klein, V. Greco, Homeostatic epidermal stem cell self-renewal is driven by local differentiation. *Cell Stem Cell* **23**, 677–686.e4 (2018).
10. M. Ito, Y. Liu, Z. Yang, J. Nguyen, F. Liang, R. J. Morris, G. Cotsarelis, Stem cells in the hair follicle bulge contribute to wound repair but not to homeostasis of the epidermis. *Nat. Med.* **11**, 1351–1354 (2005).
11. C. Blanpain, E. Fuchs, Epidermal stem cells of the skin. *Annu. Rev. Cell Dev. Biol.* **22**, 339–373 (2006).
12. J. M. Phillip, K. S. Han, W. C. Chen, D. Wirtz, P. H. Wu, A robust unsupervised machine-learning method to quantify the morphological heterogeneity of cells and nuclei. *Nat. Protoc.* **16**, 754–774 (2021).
13. A. M. Nelson, S. K. Reddy, T. S. Ratliff, M. Zulfiquer Hossain, A. S. Katseff, A. S. Zhu, E. Chang, S. R. Resnik, C. Page, D. Kim, A. J. Whittam, L. S. Miller, L. A. Garza, dsRNA released by tissue damage activates TLR3 to drive skin regeneration. *Cell Stem Cell* **17**, 139–151 (2015).
14. D. Kim, R. Chen, M. Sheu, N. Kim, S. Kim, N. Islam, E. M. Wier, G. Wang, A. Li, A. Park, W. Son, B. Evans, V. Yu, V. P. Prizmic, E. Oh, Z. Wang, J. Yu, W. Huang, N. K. Archer, Z. Hu, N. Clemetson, A. M. Nelson, A. Chien, G. A. Okoye, L. S. Miller, G. Ghiaur, S. Kang, J. W. Jones, M. A. Kane, L. A. Garza, Noncoding dsRNA induces retinoic acid synthesis to stimulate hair follicle regeneration via TLR3. *Nat. Commun.* **10**, 2811 (2019).
15. G. Wang, E. Sweren, H. Liu, E. Wier, M. P. Alphonse, R. Chen, N. Islam, A. Li, Y. Xue, J. Chen, S. Park, Y. Chen, S. Lee, Y. Wang, S. Wang, N. K. Archer, W. Andrews, M. A. Kane, E. Dare, S. K. Reddy, Z. Hu, E. A. Grice, L. S. Miller, L. A. Garza, Bacteria induce skin regeneration via IL-1β signaling. *Cell Host Microbe* **29**, 777–791.e6 (2021).
16. H. G. Augustin, G. Y. Koh, Organotypic vasculature: From descriptive heterogeneity to functional pathophysiology. *Science* **357**, eaal2379 (2017).
17. H. J. Snippert, A. Haegebarth, M. Kasper, V. Jaks, J. H. van Es, N. Barker, M. van de Wetering, M. van den Born, H. Begthel, R. G. Vries, D. E. Stange, R. Toftgård, H. Clevers, Lgr6 marks stem cells in the hair follicle that generate all cell lineages of the skin. *Science* **327**, 1385–1389 (2010).
18. A. Fullgrabe, S. Joost, A. Are, T. Jacob, U. Sivan, A. Haegebarth, S. Linnarsson, B. D. Simons, H. Clevers, R. Toftgård, M. Kasper, Dynamics of *Lgr6*$^+$ progenitor cells in the hair follicle, sebaceous gland, and interfollicular epidermis. *Stem Cell Reports* **5**, 843–855 (2015).
19. S. Huang, P. Kuri, Y. Aubert, M. Brewster, N. Li, O. Farrelly, G. Rice, H. Bae, S. Prouty, T. Dentchev, W. Luo, B. C. Capell, P. Rompolas, Lgr6 marks epidermal stem cells with a nerve-dependent role in wound re-epithelialization. *Cell Stem Cell* **28**, 1582–1596.e6 (2021).
20. K. Kizawa, M. Toyoda, M. Ito, M. Morohashi, Aberrantly differentiated cells in benign pilomatrixoma reflect the normal hair follicle: Immunohistochemical analysis of Ca^{2+}-binding S100A2, S100A3 and S100A6 proteins. *Br. J. Dermatol.* **152**, 314–320 (2005).
21. X. Wang, H. Chen, R. Tian, Y. Zhang, M. S. Drutskaya, C. Wang, J. Ge, Z. Fan, D. Kong, X. Wang, T. Cai, Y. Zhou, J. Wang, J. Wang, S. Wang, Z. Qin, H. Jia, Y. Wu, J. Liu,

S. A. Nedospasov, E. E. Tredget, M. Lin, J. Liu, Y. Jiang, Y. Wu, Macrophages induce AKT/β-catenin-dependent Lgr5$^+$ stem cell activation and hair follicle regeneration through TNF. *Nat. Commun.* **8**, 14091 (2017).
22. K. Schlegelmilch, M. Mohseni, O. Kirak, J. Pruszak, J. R. Rodriguez, D. Zhou, B. T. Kreger, V. Vasioukhin, J. Avruch, T. R. Brummelkamp, F. D. Camargo, Yap1 acts downstream of α-catenin to control epidermal proliferation. *Cell* **144**, 782–795 (2011).
23. S. Yui, L. Azzolin, M. Maimets, M. T. Pedersen, R. P. Fordham, S. L. Hansen, H. L. Larsen, J. Guiu, M. R. P. Alves, C. F. Rundsten, J. V. Johansen, Y. Li, C. D. Madsen, T. Nakamura, M. Watanabe, O. H. Nielsen, P. J. Schweiger, S. Piccolo, K. B. Jensen, YAP/TAZ-dependent reprogramming of colonic epithelium links ECM remodeling to tissue regeneration. *Cell Stem Cell* **22**, 35–49.e7 (2018).
24. I. Diamond, T. Owolabi, M. Marco, C. Lam, A. Glick, Conditional gene expression in the epidermis of transgenic mice using the tetracycline-regulated transactivators tTA and rTA linked to the keratin 5 promoter. *J. Invest. Dermatol.* **115**, 788–794 (2000).
25. M. A. Nishiguchi, C. A. Spencer, D. H. Leung, T. H. Leung, Aging suppresses skin-derived circulating SDF1 to promote full-thickness tissue regeneration. *Cell Rep.* **24**, 3383–3392.e5 (2018).
26. M. Osada, L. Jardine, R. Misir, T. Andl, S. E. Millar, M. Pezzano, DKK1 mediated inhibition of Wnt signaling in postnatal mice leads to loss of TEC progenitors and thymic degeneration. *PLOS ONE* **5**, e9062 (2010).
27. Y. M. Liang, X. L. Huang, G. Chen, L. L. Sheng, Q. F. Li, Activated hypoxia-inducible factor-1α pathway modulates early events in stretch-induced skin neovascularization via stromal cell-derived factor-1 and vascular endothelial growth factor. *Br. J. Dermatol.* **171**, 996–1005 (2014).
28. S. Joost, K. Annusver, T. Jacob, X. Sun, T. Dalessandri, U. Sivan, I. Sequeira, R. Sandberg, M. Kasper, The molecular anatomy of mouse skin during hair growth and rest. *Cell Stem Cell* **26**, 441–457.e7 (2020).
29. D. Haensel, S. Jin, P. Sun, R. Cinco, M. Dragan, Q. Nguyen, Z. Cang, Y. Gong, R. Vu, A. L. MacLean, K. Kessenbrock, E. Gratton, Q. Nie, X. Dai, Defining epidermal basal cell states during skin homeostasis and wound healing using single-cell transcriptomics. *Cell Rep.* **30**, 3932–3947.e6 (2020).
30. S. Joost, A. Zeisel, T. Jacob, X. Sun, G. L. Manno, P. Lönnerberg, S. Linnarsson, M. Kasper, Single-cell transcriptomics reveals that differentiation and spatial signatures shape epidermal and hair follicle heterogeneity. *Cell Syst.* **3**, 221–237.e9 (2016).
31. J. B. Cheng, A. J. Sedgewick, A. I. Finnegan, P. Harirchian, J. Lee, S. Kwon, M. S. Fassett, J. Golovato, M. Gray, R. Ghadially, W. Liao, B. E. Perez White, T. M. Mauro, T. Mully, E. A. Kim, H. Sbitany, I. M. Neuhaus, R. C. Grekin, S. S. Yu, J. W. Gray, E. Purdom, R. Paus, C. J. Vaske, S. C. Benz, J. S. Song, R. J. Cho, Transcriptional programming of normal and inflamed human epidermis at single-cell resolution. *Cell Rep.* **25**, 871–883 (2018).
32. D. Gao, N. Joshi, H. Choi, S. Ryu, M. Hahn, R. Catena, H. Sadik, P. Argani, P. Wagner, L. T. Vahdat, J. L. Port, B. Stiles, S. Sukumar, N. K. Altorki, S. Rafii, V. Mittal, Myeloid progenitor cells in the premetastatic lung promote metastases by inducing mesenchymal to epithelial transition. *Cancer Res.* **72**, 1384–1394 (2012).
33. L. Tong, R. M. Corrales, Z. Chen, A. L. Villarreal, C. S. De Paiva, R. Beuerman, D.-Q. Li, S. C. Pflugfelder, Expression and regulation of cornified envelope proteins in human corneal epithelium. *Invest. Ophthalmol. Vis. Sci.* **47**, 1938–1946 (2006).
34. K. Street, D. Risso, R. B. Fletcher, D. Das, J. Ngai, N. Yosef, E. Purdom, S. Dudoit, Slingshot: Cell lineage and pseudotime inference for single-cell transcriptomics. *BMC Genomics* **19**, 477 (2018).
35. S. Joost, T. Jacob, X. Sun, K. Annusver, G. L. Manno, I. Sur, M. Kasper, Single-cell transcriptomics of traced epidermal and hair follicle stem cells reveals rapid adaptations during wound healing. *Cell Rep.* **25**, 585–597.e7 (2018).
36. S. J. Ellis, N. C. Gomez, J. Levorse, A. F. Mertz, Y. Ge, E. Fuchs, Distinct modes of cell competition shape mammalian tissue morphogenesis. *Nature* **569**, 497–502 (2019).
37. S. Dekoninck, E. Hannezo, A. Sifrim, Y. A. Miroshnikova, M. Aragona, M. Malfait, S. Gargouri, C. de Neunheuser, C. Dubois, T. Voet, S. A. Wickström, B. D. Simons, C. Blanpain, Defining the design principles of skin epidermis postnatal growth. *Cell* **181**, 604–620.e22 (2020).
38. T. Tumbar, G. Guasch, V. Greco, C. Blanpain, W. E. Lowry, M. Rendl, E. Fuchs, Defining the epithelial stem cell niche in skin. *Science* **303**, 359–363 (2004).
39. S. Ohe, T. Tanaka, H. Yanai, Y. Komai, T. Omachi, S. Kanno, K. Tanaka, K. Ishigaki, K. Saiga, N. Nakamura, H. Ohsugi, Y. Tokuyama, N. Atsumi, H. Hisha, N. Yoshida, K. Kumano, F. Yamazaki, H. Okamoto, H. Ueno, Maintenance of sweat glands by stem cells located in the acral epithelium. *Biochem. Biophys. Res. Commun.* **466**, 333–338 (2015).
40. J. A. Lehoczky, C. J. Tabin, Lgr6 marks nail stem cells and is required for digit tip regeneration. *Proc. Natl. Acad. Sci. U.S.A.* **112**, 13249–13254 (2015).
41. E. M. Wier, L. A. Garza, Through the lens of hair follicle neogenesis, a new focus on mechanisms of skin regeneration after wounding. *Semin. Cell Dev. Biol.* **100**, 122–129 (2020).
42. D. Yimlamai, C. Christodoulou, G. G. Galli, K. Yanger, B. Pepe-Mooney, B. Gurung, K. Shrestha, P. Cahan, B. Z. Stanger, F. D. Camargo, Hippo pathway activity influences liver cell fate. *Cell* **157**, 1324–1338 (2014).
43. S. Dupont, L. Morsut, M. Aragona, E. Enzo, S. Giulitti, M. Cordenonsi, F. Zanconato, J. le Digabel, M. Forcato, S. Bicciato, N. Elvassore, S. Piccolo, Role of YAP/TAZ in mechanotransduction. *Nature* **474**, 179–183 (2011).
44. A. Totaro, Q. Zhuang, T. Panciera, G. Battilana, L. Azzolin, G. Brumana, A. Gandin, G. Brusatin, M. Cordenonsi, S. Piccolo, Cell phenotypic plasticity requires autophagic flux driven by YAP/TAZ mechanotransduction. *Proc. Natl. Acad. Sci. U.S.A.* **116**, 17848–17857 (2019).
45. H. J. Choi, H. Zhang, H. Park, K.-S. Choi, H.-W. Lee, V. Agrawal, Y.-M. Kim, Y.-G. Kwon, Yes-associated protein regulates endothelial cell contact-mediated expression of angiopoietin-2. *Nat. Commun.* **6**, 6943 (2015).
46. R. E. Niec, A. Y. Rudensky, E. Fuchs, Inflammatory adaptation in barrier tissues. *Cell* **184**, 3361–3375 (2021).
47. S.-Y. Chu, C.-H. Chou, H.-D. Huang, M.-H. Yen, H.-C. Hong, P.-H. Chao, Y.-H. Wang, P.-Y. Chen, S.-X. Nian, Y.-R. Chen, L.-Y. Liou, Y.-C. Liu, H.-M. Chen, F.-M. Lin, Y.-T. Chang, C.-C. Chen, O. K. Lee, Mechanical stretch induces hair regeneration through the alternative activation of macrophages. *Nat. Commun.* **10**, 1524 (2019).
48. J. E. Le Belle, N. M. Orozco, A. A. Paucar, J. P. Saxe, J. Mottahedeh, A. D. Pyle, H. Wu, H. I. Kornblum, Proliferative neural stem cells have high endogenous ROS levels that regulate self-renewal and neurogenesis in a PI3K/Akt-dependant manner. *Cell Stem Cell* **8**, 59–71 (2011).
49. G. C. Rivera-Gonzalez, B. A. Shook, J. Andrae, B. Holtrup, K. Bollag, C. Betsholtz, M. S. Rodeheffer, V. Horsley, Skin adipocyte stem cell self-renewal is regulated by a PDGFA/AKT-signaling axis. *Cell Stem Cell* **19**, 738–751 (2016).
50. C. Baumgartner, S. Toifl, M. Farlik, F. Halbritter, R. Scheicher, I. Fischer, V. Sexl, C. Bock, M. Baccarini, An ERK-dependent feedback mechanism prevents hematopoietic stem cell exhaustion. *Cell Stem Cell* **22**, 879–892.e6 (2018).
51. H. Harada, S. Itasaka, S. Kizaka-Kondoh, K. Shibuya, A. Morinibu, K. Shinomiya, M. Hiraoka, The Akt/mTOR pathway assures the synthesis of HIF-1α protein in a glucose- and reoxygenation-dependent manner in irradiated tumors. *J. Biol. Chem.* **284**, 5332–5342 (2009).
52. K. M. Dodd, J. Yang, M. H. Shen, J. R. Sampson, A. R. Tee, mTORC1 drives HIF-1α and VEGF-A signalling via multiple mechanisms involving 4E-BP1, S6K1 and STAT3. *Oncogene* **34**, 2239–2250 (2015).
53. M. Wickersham, S. Wachtel, T. Wong Fok Lung, G. Soong, R. Jacquet, A. Richardson, D. Parker, A. Prince, Metabolic stress drives keratinocyte defenses against *Staphylococcus aureus* infection. *Cell Rep.* **18**, 2742–2751 (2017).
54. T. Hirsch, T. Rothoeft, N. Teig, J. W. Bauer, G. Pellegrini, L. de Rosa, D. Scaglione, J. Reichelt, A. Klausegger, D. Kneisz, O. Romano, A. Secone Seconetti, R. Contin, E. Enzo, I. Jurman, S. Carulli, F. Jacobsen, T. Luecke, M. Lehnhardt, M. Fischer, M. Kueckelhaus, D. Quaglino, M. Morgante, S. Bicciato, S. Bondanza, M. de Luca, Regeneration of the entire human epidermis using transgenic stem cells. *Nature* **551**, 327–332 (2017).
55. G. G. Gallico III, N. E. O'Connor, C. C. Compton, O. Kehinde, H. Green, Permanent coverage of large burn wounds with autologous cultured human epithelium. *N. Engl. J. Med.* **311**, 448–451 (1984).
56. Y. Xue, X. Zhan, S. Sun, S. S. Karuppagounder, S. Xia, V. L. Dawson, T. M. Dawson, J. Laterra, J. Zhang, M. Ying, Synthetic mRNAs drive highly efficient iPS cell differentiation to dopaminergic neurons. *Stem Cells Transl. Med.* **8**, 112–123 (2019).
57. A. Dey, X. Varelas, K. L. Guan, Targeting the Hippo pathway in cancer, fibrosis, wound healing and regenerative medicine. *Nat. Rev. Drug Discov.* **19**, 480–494 (2020).
58. F. Fan, Z. He, L.-L. Kong, Q. Chen, Q. Yuan, S. Zhang, J. Ye, H. Liu, X. Sun, J. Geng, L. Yuan, L. Hong, C. Xiao, W. Zhang, X. Sun, Y. Li, P. Wang, L. Huang, X. Wu, Z. Ji, Q. Wu, N.-S. Xia, N. S. Gray, L. Chen, C.-H. Yun, X. Deng, D. Zhou, Pharmacological targeting of kinases MST1 and MST2 augments tissue repair and regeneration. *Sci. Transl. Med.* **8**, 352ra108 (2016).
59. J.-H. Lee, T. Tammela, M. Hofree, J. Choi, N. D. Marjanovic, S. Han, D. Canner, K. Wu, M. Paschini, D. H. Bhang, T. Jacks, A. Regev, C. F. Kim, Anatomically and functionally distinct lung mesenchymal populations marked by Lgr5 and Lgr6. *Cell* **170**, 1149–1163.e12 (2017).
60. T. Sato, R. G. Vries, H. J. Snippert, M. van de Wetering, N. Barker, D. E. Stange, J. H. van Es, A. Abo, P. Kujala, P. J. Peters, H. Clevers, Single Lgr5 stem cells build crypt-villus structures in vitro without a mesenchymal niche. *Nature* **459**, 262–265 (2009).
61. A. Kiemen, A. M. Braxton, M. P. Grahn, K. S. Han, J. M. Babu, R. Reichel, F. Amoa, S.-M. Hong, T. C. Cornish, E. D. Thompson, L. D. Wood, R. H. Hruban, P.-H. Wu, D. Wirtz, In situ characterization of the 3D microanatomy of the pancreas and pancreatic cancer at single cell resolution. bioRxiv 416909 (2020); https://doi.org/10.1101/2020.12.08.416909.
62. C. H. Lim, Q. Sun, K. Ratti, S. H. Lee, Y. Zheng, M. Takeo, W. Lee, P. Rabbani, M. V. Plikus, J. E. Cain, D. H. Wang, D. N. Watkins, S. Millar, M. M. Taketo, P. Myung, G. Cotsarelis, M. Ito, Hedgehog stimulates hair follicle neogenesis by creating inductive dermis during murine skin wound healing. *Nat. Commun.* **9**, 4903 (2018).
63. R. Satija, J. A. Farrell, D. Gennert, A. F. Schier, A. Regev, Spatial reconstruction of single-cell gene expression data. *Nat. Biotechnol.* **33**, 495–502 (2015).

64. U. Raudvere, L. Kolberg, I. Kuzmin, T. Arak, P. Adler, H. Peterson, J. Vilo, g:Profiler: A web server for functional enrichment analysis and conversions of gene lists (2019 update). *Nucleic Acids Res.* **47**, W191–W198 (2019).

Acknowledgments: We thank H. Zhang of the Bloomberg Flow Cytometry and Immunology Core for helping us with the flow cytometry sorting; H. Hao, L. Orzolek, and C. Talbot at the Johns Hopkins Transcriptomics and Deep Sequencing Core with the microarray and single-cell sequencing experiments; J. Rothstein of the Johns Hopkins University for the use of $Lgr6^{cre}$ mice; and S. Millar of the Icahn School of Medicine at Mount Sinai and A. Glick of the Penn State University for the use of the Krt5-rtTA mouse line. **Funding:** Research reported in this publication was supported by the National Institute of Arthritis and Musculoskeletal and Skin Diseases, part of the National Institutes of Health, under 1F32AR074865-01 to E.W. and R01AR064297/AR068280 to L.A.G. and the Maryland Stem Cell Research Fund Award 2020-MSCRFL-5375 to S.K.R. **Author contributions:** Conceptualization: S.K.R., L.A.G., and Y.X. Methodology: S.K.R., L.A.G., Y.X., C.Ly., A.V.E., A.K., Y.C., N.K., D.H., E.W., S.W., S.L., A.L., C.K., G.W., P.-H.W., and D.W. Investigation: Y.X., C.Ly., A.V.E., A.K., Y.C., A.T., C.Le., and L.H. Visualization: Y.X., C.Ly., A.V.E., A.K., Y.C., A.T., C.Le., L.H., and C.K. Funding acquisition: S.K.R. and L.A.G. Project administration: S.K.R., L.A.G., and Y.X. Supervision: S.K.R. and L.A.G. Writing—original draft: S.K.R., L.A.G., Y.X., C.Ly., A.V.E., and A.K. Writing—review and editing: S.K.R., L.A.G., Y.X., C.Ly., A.T., A.V.E., A.K., G.W., and D.W. **Competing interests:** The authors declare that they have no competing interests. **Data and materials availability:** All data needed to evaluate the conclusions in the paper are present in the paper and/or the Supplementary Materials. The microarray and single-cell sequencing data discussed in this publication have been deposited in NCBI's Gene Expression Omnibus and are accessible through GEO series accession number GSE186774.

Submitted 11 August 2021
Accepted 10 March 2022
Published 27 April 2022
10.1126/sciadv.abl8698